

**Polyatomic bismuth impacts into germanium: Molecular dynamics study**Christian Anders,<sup>1</sup> Karl-Heinz Heinig,<sup>2</sup> and Herbert M. Urbassek<sup>1,\*</sup><sup>1</sup>*Physics Department and Research Center OPTIMAS, University Kaiserslautern, Erwin-Schrödinger-Straße, D-67663 Kaiserslautern, Germany*<sup>2</sup>*Institute of Ion Beam Physics and Materials Research, Helmholtz-Zentrum Dresden-Rossendorf, P. O. Box 510119, D-01314 Dresden, Germany*

(Received 23 April 2013; revised manuscript received 11 June 2013; published 26 June 2013)

Using molecular dynamics simulations, we study the effects induced by the impact of  $\text{Bi}_n$  ( $n \leq 5$ ) clusters with energies in the range of a 3–20 keV/atom into a Ge target. The target consists of Ge including a 10% contribution of randomly distributed Bi atoms. The impacting polyatomic clusters create a long-lived melt pool at the surface. After resolidification, the surface shows a characteristic meniscuslike depression; it is caused both by the missing sputtered atoms and by the volume change of Ge upon melting and amorphization. During cooling, Bi is driven towards the center of the melt pool. A large precipitate forms at the surface (for polyatomic impact) or in the center of the molten pocket (for monatomic impact). The remainder of the resolidified amorphous zone is purified from Bi. We argue that the reason for the demixing of Bi and Ge is the thermophoretic or Soret effect which is caused by the different diffusivities of Bi and Ge in the melt. Bi is sputtered preferentially from the sample. The extent of surface modification, the amount of Bi collected on the surface, the concentration of Bi, and structure of Bi precipitates in the former melt pool are analyzed in their dependence on projectile size, impact energy, and direction.

DOI: [10.1103/PhysRevB.87.245434](https://doi.org/10.1103/PhysRevB.87.245434)

PACS number(s): 79.20.Ap, 61.80.Lj, 79.20.Rf

**I. INTRODUCTION**

Ion-induced modification of surfaces is of interest for a variety of applications including surface erosion and surface nanopatterning. In recent years, the formation of ion-induced structures on the surface (for example, ripples or nanodots) has been vividly investigated due to its prospects of forming controlled periodic surface structures. Even in apparently simple systems, such as pure semiconductors, the nanopatterns formed show a rich array of structures depending on the ion species and energy employed and on the impact angle.<sup>1–5</sup>

Aside from monatomic ions, also polyatomic cluster ions can be used for surface modification. A widespread cluster source generates  $\text{Bi}_n$  clusters ( $n = 1–3$ ).<sup>6</sup> While these clusters are often used for surface analysis, such as secondary ion mass spectrometry (SIMS),<sup>7,8</sup> recently ideas have been forwarded to investigate in how far Bi cluster ions may influence the surface patterning of surfaces.<sup>9–11</sup> Experiments report ordered arrays of nanodots with good near order and high amplitude of the dots. The dots are found to be enriched by the implanted Bi. Motivated by these developments, we investigate here the effects of Bi cluster impacts into a mixed Ge/Bi target.

Due to their high mass, the Bi projectiles will be implanted in the target. Thus, at higher ion fluences, the projectile will not impact into pure Ge but rather into a Ge-Bi mixture. Since Ge and Bi are not miscible, the local composition of the target will be strongly inhomogeneous. *A priori* it is unclear what the near-surface composition will look like. We therefore use a simple model in which a homogeneous mixture of 10% Bi in Ge will be investigated. While such a mixture may appear unrealistic, it will serve as a reference target to study the effects of ion impact. The segregation of Bi and the local amorphization in the target can thus be studied in dependence of the cluster impact energy and the cluster size. The results will be useful for future work on modeling the fluence-dependent morphology changes in a Ge target

under Bi cluster ion impact. We note that in a recent paper, the effects of polyatomic  $\text{Bi}_N$  impact into Si were studied.<sup>12</sup> There, the Bi precipitation developing in the sample could be observed.

Our study shows that polyatomic  $\text{Bi}_N$  ion impact creates a long-lived ( $> 100$  ps) melt pool at the surface. The formation of the melt pool has several interesting consequences. First, it provides a high-mobility environment in which Bi can efficiently precipitate and migrate to the surface; we shall argue that the cause of the drift to the surface is the so-called Soret effect. Second, the melt pool smoothens the surface. In fact, the surface acquires a shape of minimum curvature; its radius of curvature is the same in all directions, even for oblique ion impact. This smoothing mechanism has not been described before in the literature. We presume that it will play an important role under prolonged ion bombardment and needs to be taken into account when modeling pattern formation under heavy polyatomic impact.<sup>12</sup> We shall analyze this role in detail elsewhere.

**II. METHOD**

We use the parallelized molecular dynamics simulation package LAMMPS (Ref. 13) for our study.

**A. Interaction potentials**

The interaction between Ge atoms is modeled by a modified Stillinger-Weber potential created by Posselt and Gabriel.<sup>15</sup> It gives the lattice constant  $a = 5.654$  Å, the density of  $n_s = 0.0443$  Å<sup>-3</sup>, and the cohesive energy  $E_{\text{coh}} = 3.86$  eV in good agreement with experiment. The melting temperature amounts to  $T_m = 1310$  K, which is slightly above the experimental value of 1211 K; the liquid has a density which is 10% above the solid density. The properties of the amorphous phase have been investigated in Ref. 15 and have been found to be

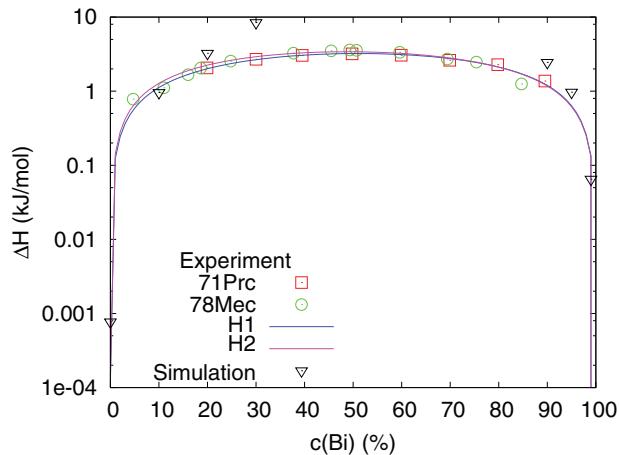


FIG. 1. (Color online) Mixing enthalpy  $\Delta H$  of a homogeneous Ge-Bi mixture containing a Bi atom concentration  $c$ . Experimental data taken from Ref. 14: H1 and H2 denote two analytical fits presented there, while 71 Prc and 78 Mec are original experimental data. Simulation data are calculated from the potential presented in this work.

reasonable in comparison to experiment; the density of  $a$ -Ge is predicted to be  $n_a = 0.0434 \text{ \AA}^{-3}$ , 2% below the crystalline density  $n_s$ .

The Bi-Bi interaction potential is taken from the work of Yan *et al.*,<sup>16</sup> who set it up for describing the immiscible Cu-Bi system. It is a many-body potential of the Finnis-Sinclair<sup>17</sup> type. The cohesive energy of Bi amounts to 2.17 eV; the melting temperature is 544 K.<sup>14</sup>

The modeling of the Bi-Ge interaction is nontrivial since the Bi-Ge system is immiscible.<sup>14</sup> In this work, we are mainly interested in the demixing (segregation) of Bi from Ge, which is controlled by the heat of mixing. We therefore adopted a simple approach, in which the Ge-Bi interaction is represented by a Stillinger-Weber potential as for the Ge-Ge interaction. We only change the bond energy (parameter  $\epsilon$  in the potential) from its value 1.93 eV characterizing Ge to 1.36 eV in order to fit the mixing enthalpy of a random  $\text{Bi}_{0.1}\text{Ge}_{0.9}$  alloy. This means that the energetics of the Bi-Ge interaction is taken into account, but structural effects are ignored; in our model the Bi-Ge bonding is tetrahedral as in Ge. We note that for the effects modeled in this paper (ion-beam-induced melting and segregation), the correct modeling of the melting temperatures and of the heat of mixing are essential; these have been included in our potential.

Figure 1 plots the heat of mixing obtained for our system. Here, metastable random Ge-Bi alloys with Bi atomic number concentration  $c$  have been constructed and the heat of mixing has been calculated using the procedure of Ref. 18. We see that our potential allows us to describe the heat of mixing satisfactorily up to concentrations of  $\sim 20\%$ . This covers the range of interest in this work.

All potentials used here are fitted to a Ziegler-Biersack-Littmark (ZBL) potential<sup>19</sup> at large repulsive energies to describe close collisions. Figure 2 shows the three interaction potentials used and their smooth transition to the high-energy ZBL potential.

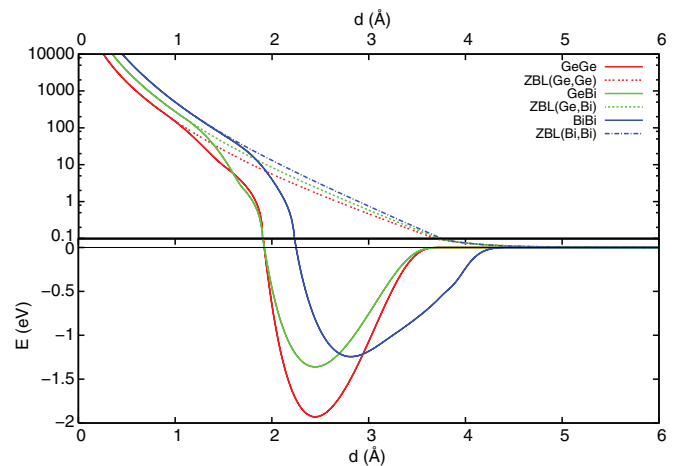


FIG. 2. (Color online) Dimer interaction potentials for Ge and Bi (full) and repulsive high-energy ZBL potentials (dotted). Note the change of the ordinate energy scale from linear in the attractive part to logarithmic in the repulsive part.

## B. System

The target has a diamond structure with a (100) surface. It contains 10% Bi atoms which are set on random lattice sites. The target temperature is set to 300 K and thermalized for 1000 time steps, before the projectile is started. The target typically has a depth of 170  $\text{\AA}$ , and a lateral size of 340  $\text{\AA}$ ; for high-energy impacts the target size has been increased.

At the bottom and the lateral sides we use boundaries thermostatted to 300 K. In these, a volume with a thickness of one lattice constant  $a$  is subject to the Berendsen thermostat.<sup>20</sup> The Berendsen relaxation time  $\tau$  is defined as the time necessary to equilibrate the difference of the average temperature in the boundary zone and the thermostat temperature. According to the heat conduction equation, this time depends on the width of the boundary zone  $a$  as  $a^2/\kappa$ ,<sup>21</sup> where  $\kappa = 3.66 \times 10^{-5} \text{ m}^2 \text{ s}^{-1}$  is the thermal diffusivity of Ge at 300 K.<sup>22</sup> We thus obtain  $\tau = a^2/\kappa = 8.7 \text{ fs}$ . The surface at which the Bi cluster impacts is left free; here and in the bulk of the target, an NVE simulation is run to allow unbiased impact dynamics. Later when the impact phase is over (after 20 ps for  $\text{Bi}_1$  and after 50 ps for  $\text{Bi}_5$  impact), the thermostat region is extended to five lattice constants to guarantee for a realistic cooling of the target to the ambient temperature of 300 K.

We employ an adaptive time step. It is chosen such that an atom moves at most  $0.005a$  during a time step; in addition, it is not allowed to exceed 1 fs. Simulations are terminated when the temperature in the specimen has fallen everywhere below the melting temperature of Ge. For our smallest simulation ( $\text{Bi}_1$  impact at 3 keV/atom), this happens at 30 ps, while for the larger clusters it will exceed 500 ps.

The target is irradiated by  $\text{Bi}_N$  clusters containing  $N = 1-5$  atoms. The energy per cluster atom  $E$  was varied in the range of  $E = 3-20 \text{ keV/atom}$ . Usually, the clusters impinge in the direction of the surface normal. Additionally, oblique impacts were simulated at  $25^\circ$  for  $E = 10 \text{ keV/atom}$  and at  $45^\circ$  for  $E = 20 \text{ keV/atom}$  for  $N = 1$  and 3. The clusters have the form of a unilateral triangle ( $N = 3$ ), a tetramer ( $N = 4$ ),

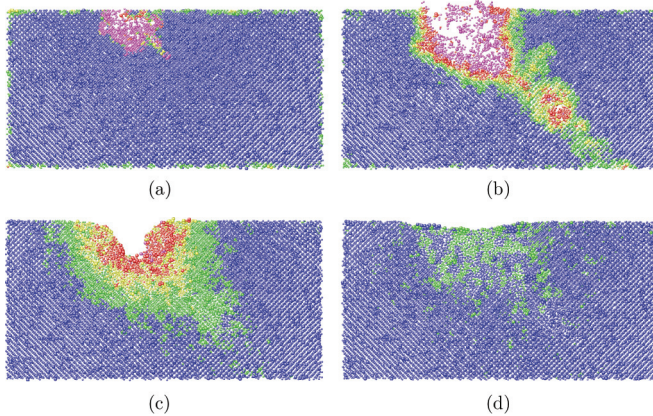


FIG. 3. (Color online) Snapshots showing the time evolution of the target after oblique impact of a  $\text{Bi}_3$  cluster at  $25^\circ$  with 10 keV/atom. (a) 0.11 ps, (b) 1.55 ps, (c) 20.2 ps, (d) 610 ps after impact. Colors denote local temperatures. Violet: above the vaporization temperature of Ge,  $>3103$  K. Red: above the vaporization temperature of Bi,  $>1833$  K. Yellow: above the melting temperature of Ge,  $>1211$  K. Green: above the melting temperature of Bi,  $>544$  K. Blue: solid.

and a trigonal bipyramid ( $N = 5$ ). These structures have been energy minimized to obtain the equilibrium geometry.

### III. RESULTS

#### A. Temporal evolution

Figure 3 visualizes four characteristic stages following a  $\text{Bi}_3$  cluster impact. The impact creates a collision cascade in the target which is present for less than 1 ps [Fig. 3(a)]. The high energy density delivered to the target disrupts the surface and sputters several atoms [Fig. 3(b)], leaving the remaining energized volume in the liquid state. Due to the high energy density delivered, a temporary crater forms at the surface in the heated zone [Fig. 3(c)]. While the material is still molten, the capillary forces will smoothen the surface. The cooling and solidification of the melt pool require long times whose exact amount depends on cluster size and impact energy [Fig. 3(d)]. After freezing, the former melt pool is left in an amorphous structure.

A particularly prominent feature of the impact is the formation of a depression in the final surface, which we shall denote as a *meniscus*. This meniscus receives its regular form from the fact that the hemispherical liquid slowly cools and can therefore attain its equilibrium structure which is characterized by the minimization of the surface curvature (cf. also the discussion following). The size of the meniscus depends on both the sputter yield and the volume change of the irradiated material due to amorphization. After prolonged irradiation, the size of the meniscus will only depend on the sputter yield since the atomic density of the material will have saturated.

We note that the formation of the meniscus will lead to the evolution of pronounced surface structures after continuing impacts. We shall discuss these effects in combination with experimental work elsewhere. These general features, i.e., collision cascade, melt pool formation, resolidification to an

amorphous zone, formation of a meniscus at the surface, hold true for all combinations of cluster sizes and impact energies studied here.

#### B. Dependence on cluster size and energy

We now discuss the target modifications induced by cluster impact in their dependence on cluster size and energy. We use the amorphization detector of Ref. 15 to characterize the zone damaged by the  $\text{Bi}_N$  cluster impact. The array of snapshots displayed in Fig. 4 shows the crystal structure of the cooled target (300 K) by a color code:

(i) yellow denotes atoms which have four neighbors; this includes atoms in undamaged diamond structure, but also slightly damaged structures, in which at least one angle deviates from the ideal tetrahedral angle;

(ii) blue denotes atoms which do not have four neighbors.

Thus, the blue area shows the zone amorphized by the impact. The analysis of the computer-generated movies of the structure evolution demonstrates that the atoms marked “blue” (in the amorphous state) will not recrystallize.

##### 1. Monomer and dimer impact

The first column of Fig. 4 shows the effect of the input energy for monomer ions. At the lowest impact energy of 3 keV, the impact damage (i.e., the amorphized zone) is located at the surface. With increasing impact energy, this zone extends further into the target. Because of the statistical nature of the individual atomic collisions, the damage induced can greatly vary even for the same impact energy depending on the exact location of the impact point. The large mass of the impinging Bi ion leads in some cases to elongated track structures leading deep into the target. However, due to collision statistics, in other cases the energized zone remains close to the surface; this is the case for the 20-keV impact. We find that proper Bi ion channeling is not particularly pronounced; this is due to the large ion size, the nonzero target temperature, and in particular the fact that the target is a Ge-Bi alloy and hence the channels are not uniform.

Dimer impacts (second column in Fig. 4) lead to similar damage structures as monomer impact. The formation of elongated damage tracks in the target becomes even more pronounced.

We thus conclude that for monomer and dimer impact, the melt pools often appear along the energized track far from the surface. This means that also the effects in the melt pool such as amorphization and segregation (see below) of Bi will appear inside buried molten pockets rather than at the surface. While this might be not so interesting for surface modification, it has consequences for the stability of the bulk material and for followup impacts when predamaged (i.e., segregated and amorphized) regions are subjected to further irradiation.

##### 2. Polyatomic cluster ( $N \geq 3$ ) impact

Columns 3–5 of Fig. 4 display the targets after impact of clusters of size  $N = 3$ –5. The effect of polyatomic cluster impact is always similar: the creation of a melt pool close to the surface whose size increases with projectile size and

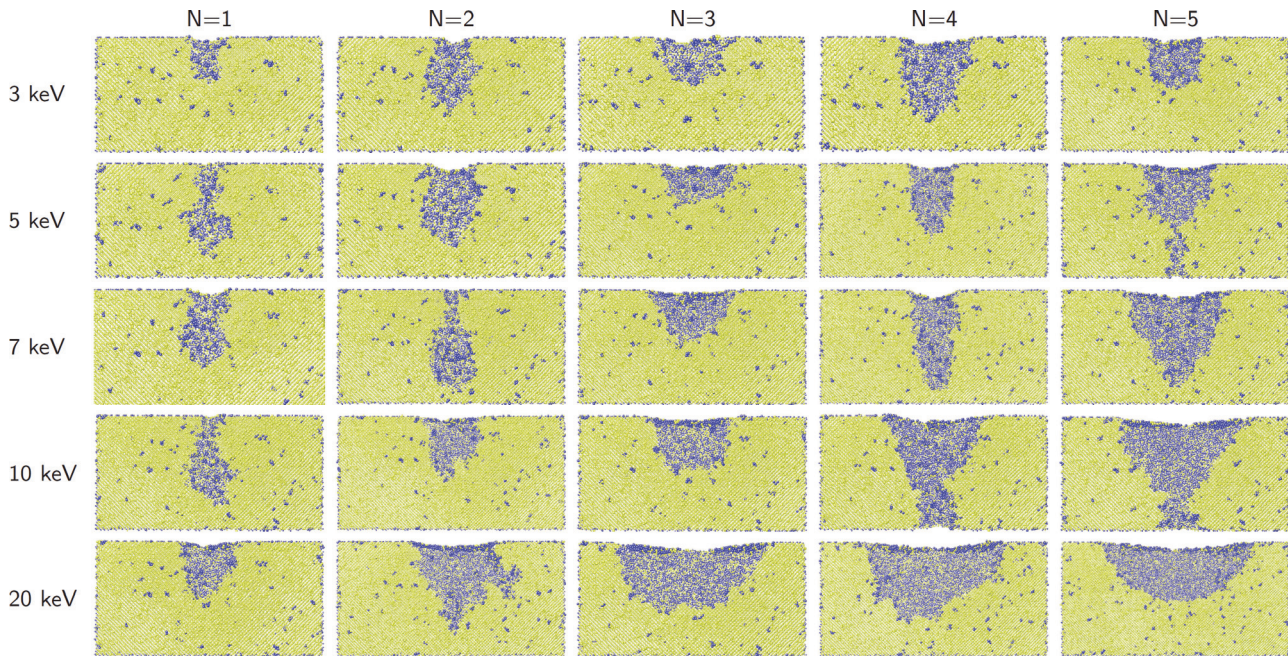


FIG. 4. (Color online) Final damage structures created. Projectile size ( $N = 1-5$ ) increases from left to right, and energy ( $E = 3, 5, 7, 10, 20$  keV/atom) increases from top to bottom. Colors denote degree of amorphization, from not or only slightly damaged (yellow) to amorphous (blue) (see Sec. III B).

energy. Since the cluster is too big to channel between the target atoms, it deposits all its energy near the surface; so the melt pool for clusters with  $N \geq 3$  is located at the surface.

An approximately hemispherical region around the impact point becomes molten by the cluster impact. As a consequence, a meniscus is seen in the resolidified target surfaces (Fig. 4). As discussed above, the origin of this meniscus is in the melt pool formed after impact; since the liquid has a higher density than the solid, the capillary forces will minimize the surface and create a concave surface structure. This structure is frozen in during the resolidification and is clearly seen in all pictures where a melt pool has been generated (Fig. 4).

### C. Oblique impact

The properties of the meniscus are further clarified by studying off-normal impact. We simulated oblique impacts for a  $\text{Bi}_1$  monomer and for a  $\text{Bi}_3$  cluster, both for 10 and 20 keV/atom.

In Fig. 5, we display the final state obtained for oblique impact of a  $\text{Bi}_3$  cluster from two different perspectives: along and perpendicular to the projected ion impact direction. The time evolution of the 10-keV impact [Fig. 5(a)] was already shown in Fig. 3. The important point to note here is that the curvature radius of the meniscus is the same when measured along the ion-beam direction and perpendicular to it. This proves that the meniscus has attained a spherical form; the action of the surface capillary forces has given it the form of a minimal surface with a unique radius of curvature in all directions. If the meniscus had formed during the ion-bombardment phase, it must have been expected that the meniscus would have adopted an elliptic form, elongated in the direction of the ion impact; note that the damage structure inside the target is indeed not hemispherical. However, by the

action of the capillary forces in the melt pool, the surface has attained a state of equal curvature in all directions. The form of the meniscus only depends on the lateral size of the melt pool and the missing volume, but not on details of the incidence geometry.

A second noteworthy feature is the fact that the center of the meniscus is shifted downward with respect to the ion impact point. This becomes particularly clear for larger incidence angles [see Fig. 5(b)]. This asymmetry of the melt pool is equivalent to a net mass flow of target atoms which needs to be taken into account when describing the high-fluence evolution of the target.<sup>12</sup>

### D. Bi segregation

In the melt pool, the Ge and Bi atoms become mobile and change positions to find energetically preferred neighbor atoms. We show in Fig. 6 the melt pool during and after solidification by highlighting the atom species. In the final state, after resolidification, the former melt pool has become almost entirely depleted of Bi; the Bi atoms have been driven to the surface where a large Bi precipitate has appeared.

Several mechanisms may be invoked to be responsible for this demixing process:

(i) Due to the positive heat of mixing, Bi and Ge atoms tend to segregate; this is possible in the liquid with its increased atom mobility. Since Bi has a lower melting point (544 K) than Ge (1211 K), Bi moves away from the resolidification front; this is sometimes called the process of the zone purification. Note that above 1211 K, Bi and Ge are freely miscible in the liquid phase; below this temperature, miscibility only occurs in a narrow band close to  $c = 100\%$  Bi concentration.

(ii) Bi has a lower surface energy,<sup>23,24</sup> and thus Bi prefers to be situated at the surface.

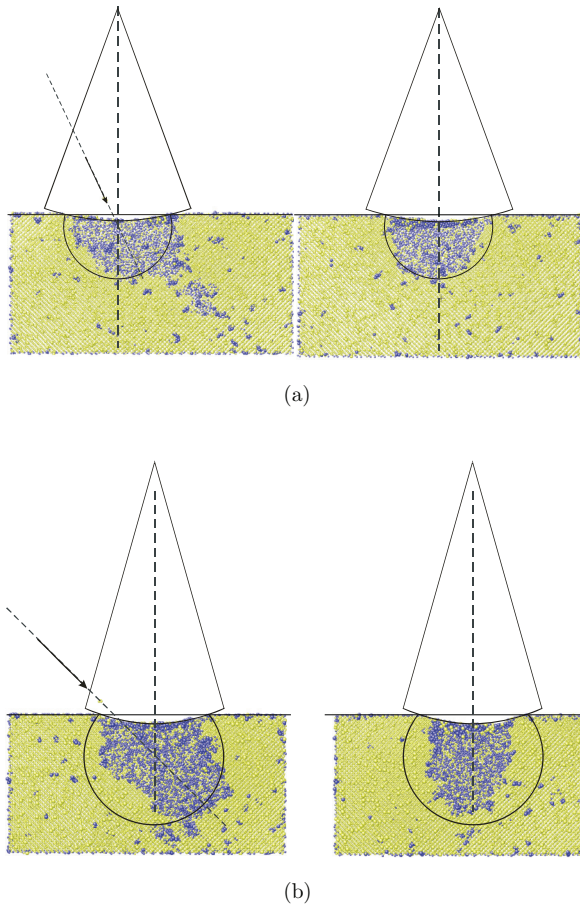


FIG. 5. (Color online) Surface depression (meniscus) formed after impact of a  $\text{Bi}_3$  cluster at oblique incidence: (a) at  $25^\circ$ , 10 keV, (b) at  $45^\circ$  to the surface normal, 20 keV. Cross-sectional views along (right) and perpendicular (left) to the ion impact direction. The curvature radius of the meniscus, the ion impact direction, and the surface normal are highlighted. Colors denote degree of amorphization, from not or only slightly damaged (yellow) to amorphous (blue) (see Sec. III B).

(iii) Finally, the difference in diffusivity, and in particular in the temperature dependence of diffusivity, of Bi and Ge in the melt provides for a drift. The faster diffusing species is driven along the temperature gradient towards the hottest zone, which is in our case at the surface, farthest away from the resolidification front. While we have no data available for the (temperature-dependent) diffusivities of Ge and Bi in the liquid, we argue that diffusivities are higher for lower-melting materials, and that hence Bi has a considerably higher diffusivity as compared to Ge.<sup>25</sup> In summary, this effect gives rise to a strong directed flux of Bi to the surface. This effect has been termed thermophoresis in gases, and the Soret effect in liquids.<sup>26–31</sup>

As the time dependence of the demixing process in Fig. 6 shows, the motion of clusters towards the surface is not of a diffusive nature, but shows clear signs of a convective drift. This finding immediately excludes the option (ii) above since the difference in surface energies acts as a boundary condition to the diffusion flux, but not as a directed force acting inside the material. The process of zone purification would lead to a

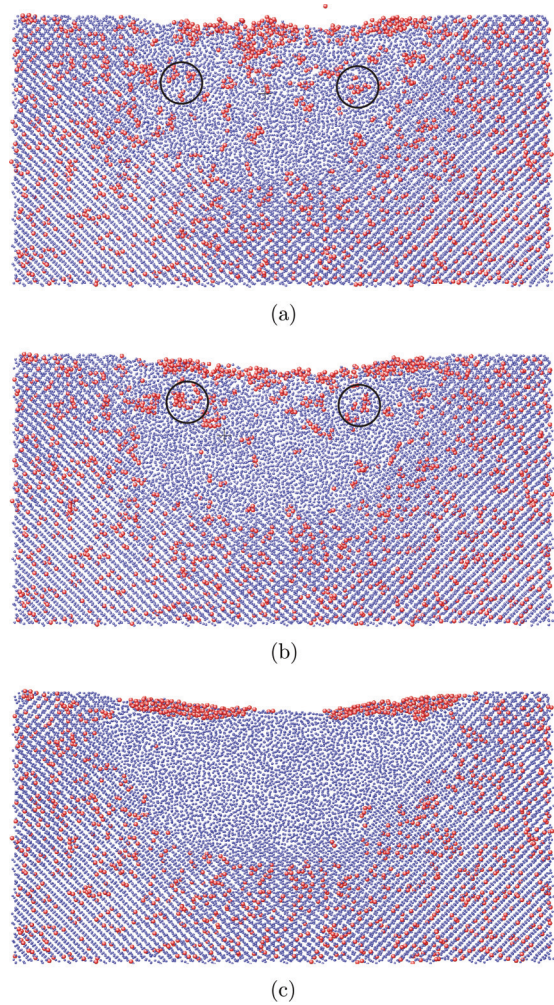


FIG. 6. (Color online) Temporal evolution of the target after impact of a  $\text{Bi}_3$  cluster at 20 keV/atom: (a) 72 ps, (b) 100 ps, (c) 584 ps. Colors denote atom species (red: Bi, blue: Ge) and highlight atom segregation after impact. The circles enclose Bi precipitates which drift to the surface. In the final structure (c) the former melt pool is cleaned of Bi.

Bi enrichment close to the resolidification front; this, however, is not seen in the snapshots, and so we also have to dismiss option (i). We hence conclude that the demixing process seen in our simulations appears to constitute an example of the Soret effect occurring in liquids. It is very pronounced here since the temperature gradient is large, and the spatial and temporal scales are very small.

While this study provides a clear indication that segregation is caused by the Soret effect, further investigations and experimental support would be welcome.

### E. Bi precipitation

During the demixing process, large Bi aggregates develop which we shall term Bi precipitates. We use a cluster detector according to Ref. 32 with the distance limit set to  $3.565 \text{ \AA}$  to determine the number and size of the Bi precipitates present in our Ge target before and after impact. Figure 7 displays the largest Bi precipitate found by this detector for several cluster sizes at 10 keV/atom impact energy. While for the

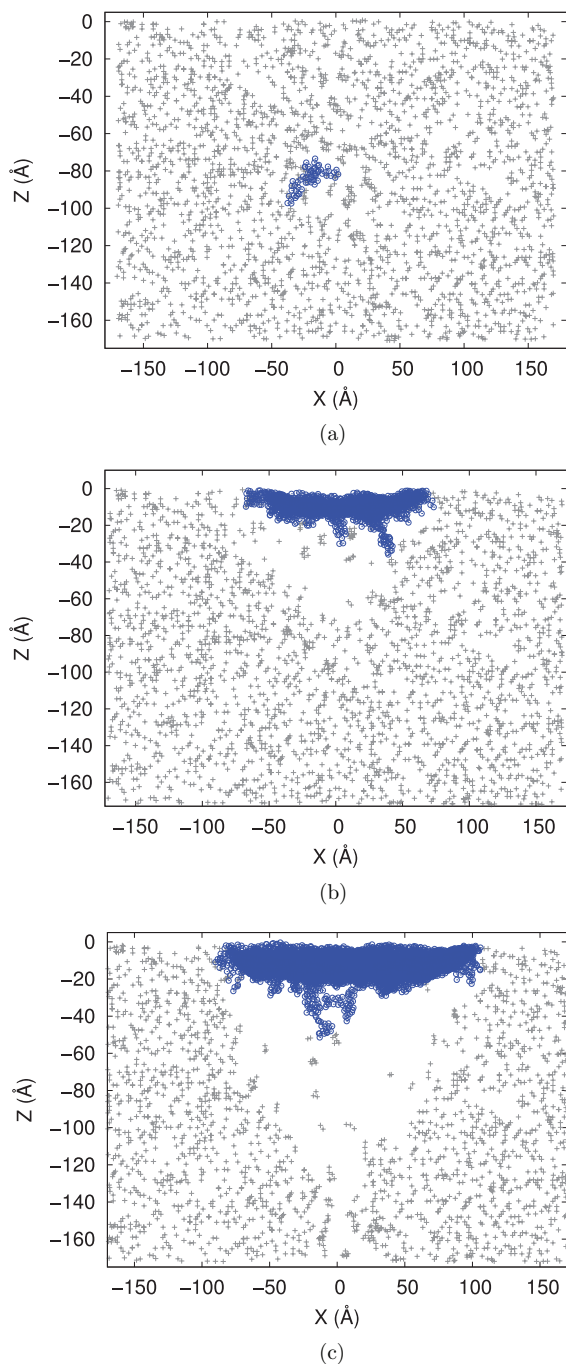


FIG. 7. (Color online) Largest Bi precipitate caused by segregation. (a)  $\text{Bi}_1$  impact at 10 keV. (b)  $\text{Bi}_3$  impact at 10 keV/atom. (c)  $\text{Bi}_5$  impact at 12 keV/atom. The largest precipitates have sizes of 61, 2243, and 7711 Bi atoms, respectively. Gray symbols denote Bi atoms not belonging to the largest precipitate.

monomer impact the largest Bi precipitate grows in a molten pocket inside the target, polyatomic cluster impact leads to the largest Bi precipitate growing at the surface. This finding nicely illustrates the role of the temperature gradient in defining the position of the growing Bi precipitate: The thermophoretic effect always drives Bi in the direction of the temperature gradient, such that the precipitate grows at the location of the temperature maximum. For polyatomic cluster impact, this is

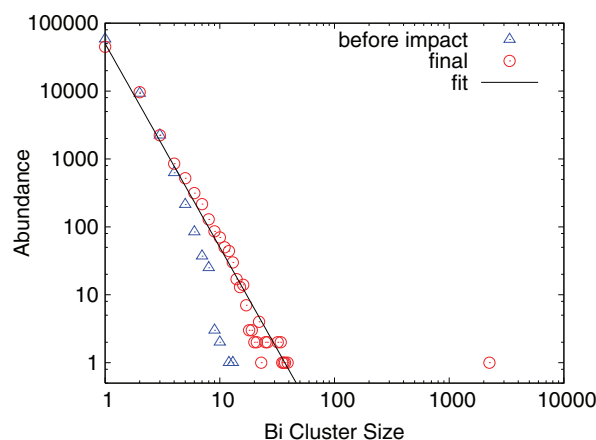


FIG. 8. (Color online) Size distribution of Bi precipitates in the target impacted with  $\text{Bi}_3$  at 10 keV/atom.

found at the surface, while for monatomic impacts, it is often located buried in the target (cf. Fig. 4).

Figure 8 shows the size spectrum of the Bi precipitates for the particular case of  $\text{Bi}_3$  impact at 10 keV/atom. Here, we define the abundance or size distribution  $f(N)$  as the (average) number of precipitates of size  $N$ ; it fulfills the mass conservation law (apart from sputtering)  $\sum Nf(N) = N_{\text{Bi}}$ , where  $N_{\text{Bi}}$  is the number of Bi atoms in the simulation.

While the initial size distribution is a bit steeper, the abundance of the precipitate size  $N$  after the impact can be fitted to an  $N^{-3}$  power law. The most important effect of the segregation process, however, is that one very large precipitate with  $N \cong 2000$  is created; it is the one seen at the top of the melt pool in Fig. 7(b). We would welcome to obtain experimental data on the presence and size of Bi precipitates developing under polyatomic Bi impact into Ge. Note that for comparable impact conditions into a Si target, such precipitates have already been found.<sup>12</sup>

Figure 9 presents the dependence of the size of the largest precipitate on impact energy and impact cluster size. We observe the general trend that the size of the largest Bi precipitate formed in the melt pool increases with impact energy and cluster size. Due to the increasing size of the melt

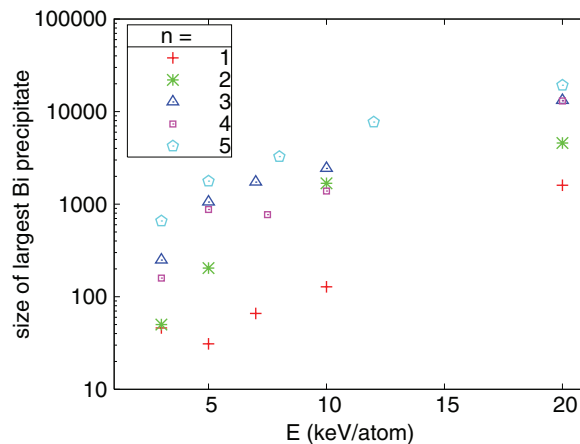


FIG. 9. (Color online) Sizes of largest Bi precipitate as a function of impact cluster size and energy (perpendicular impact).

pool, and its long lifetime, the largest melt pool created for  $\text{Bi}_5$  impact at 20 keV/atom creates a precipitate with size of  $N \cong 20\,000$ .

### F. Sputtering

Due to the cluster impacts, material is sputtered from our target. We denote the number of sputtered Bi (Ge) atoms as  $Y_{\text{Bi}}$  ( $Y_{\text{Ge}}$ ) and the total yield as  $Y = Y_{\text{Ge}} + Y_{\text{Bi}}$ . The sputter yields are subject to fluctuations; if the same projectile cluster impinges with the same energy on a different impact point at the surface, the yield will in general vary. Sputter-yield fluctuations are of the order of the average yield itself,<sup>33,34</sup> but decrease with increasing cluster size.<sup>35</sup> We investigated the influence of statistics for the particular case of  $\text{Bi}_3$  cluster impact with 10 keV/atom at  $25^\circ$  impact angle, where we ran three simulations. The averaged sputter yield results in  $45 \pm 26$  emitted atoms per projectile atoms. Experimental yields<sup>36</sup> amount to  $Y = 28$  for perpendicular impact and  $Y = 30$  for oblique impact at  $25^\circ$ ; this is within the  $1\sigma$  standard deviation of our simulation result. For the  $\text{Bi}_1$  monomer only one impact was simulated; the yield was 25 atoms.

Figure 10(a) shows the total sputter yields. While monatomic  $\text{Bi}_1$  impact leads to moderate sputtering of the

order of 10 or less atoms, polyatomic impact creates sizable sputter yields; in the case of the highest-energy deposition ( $\text{Bi}_5$  impact at 20 keV/atom), more than 1000 atoms are emitted. Note that sputter yields increase both with energy and cluster size; deviations from this rule are owed to our small statistics; the data presented in Fig. 10 are based on a single simulation in each case.

Figure 10(b) shows the ratio of sputtered Bi to sputtered Ge atoms. A naive view would expect stoichiometric sputtering, that is,  $Y_{\text{Bi}}/Y_{\text{Ge}} = c_{\text{Bi}}/c_{\text{Ge}} = 0.1/0.9 = 0.11$ . Our data are far from this naive prediction and show that Bi is sputtered preferentially. Due to the limited statistical basis of our simulations, it appears not possible to evaluate the energy and impact-energy dependence of the sputter preferentiality; an average value appears to lie between  $Y_{\text{Bi}}/Y_{\text{Ge}} = 0.2$  for  $\text{Bi}_5$  and 0.5 for  $\text{Bi}_2$  impact.

Analytical sputter theory has long pinned down the major causes for deviations from stoichiometric sputtering: the more weakly bound species and the lighter species are preferentially sputtered.<sup>37–39</sup> Here, the effect of binding energy is stronger, while the mass effect is weak. We thus conclude that, while Bi is almost three times heavier than Ge, it is the weaker bonding which leads to its preferential emission. Finally, it might be argued that the fact that Bi segregates to the surface might be the cause for its preferential emission; however, segregation occurs on time scales of 100 ps (see Fig. 6), while sputtering is terminated after a few or at most a few 10 ps. We hence can rule out Bi surface segregation as the cause for its preferential sputtering.

### IV. SUMMARY

We studied the modifications induced by energetic Bi cluster impact into a random  $\text{Bi}_x\text{Ge}_{1-x}$  alloy, with concentration  $x = 0.1$ . We found the following characteristic features.

(1) In the collision cascade region, the target melts. In particular for larger clusters and at higher impact energies, the melt pool is extended and cools only slowly, on the time scale of 100 ps or more.

(2) For polyatomic impact, the melt pool has a hemispherical geometry with its largest cross section at the surface. For monatomic, and to a lesser degree, for diatomic, impact, the melt pool may be buried beneath the surface.

(3) Upon cooling, the melt solidifies in the amorphous state. Due to the higher density of the liquid phase, and due to the atoms missing due to sputtering, a meniscuslike surface depression develops on the surface.

(4) During cooling, Bi is driven towards the center of the melt pool. A large precipitate forms at the surface (for polyatomic impact) or in the center of the molten pockets (for monatomic impact). The remainder of the resolidified amorphous zone is purified from Bi.

(5) We argue that the reason for the demixing of Bi and Ge is the thermophoretic or Soret effect which is caused by the different diffusivities of Bi and Ge in the melt.

(6) The size of the largest Bi precipitate formed during segregation increases with impact energy and projectile size.

(7) If monatomic  $\text{Bi}_1$  is used as a projectile, an elongated melt structure following the projectile slowing-down path

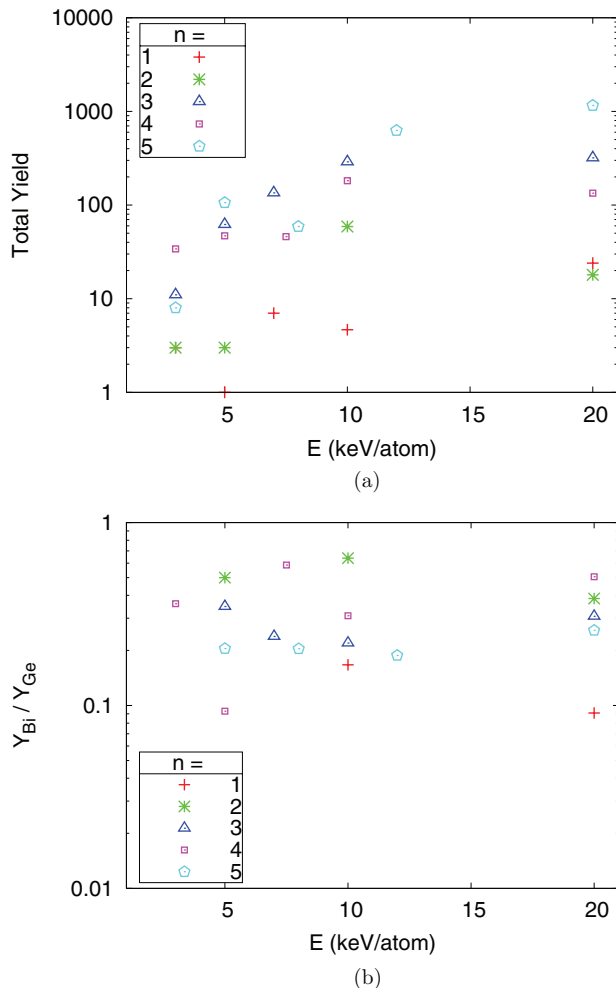


FIG. 10. (Color online) (a) Total and (b) relative sputter yields for perpendicular incidence.

forms; the path length increases with the projectile energy. Bi segregates in several pockets along this track.

(8) Bi is sputtered preferentially from the mixture; this is caused by its smaller surface binding energy.

The melt pool that develops under polyatomic heavy-ion impact smoothens the surface. In addition, for oblique ion impact, the center of the meniscus is shifted downward with respect to the ion impact point. This asymmetry of the melt pool is equivalent to a net mass flow of target atoms. These features have not been described before in the literature.

We presume that they will play an important role under prolonged ion bombardment and need to be taken into account when modeling pattern formation under polyatomic heavy-ion impact.

#### ACKNOWLEDGMENT

This work has been supported by the *Deutsche Forschungsgemeinschaft* via the Research Unit 845 *Self-organized nanostructures induced by low-energy ion beam erosion*.

\*urbassek@rhrk.uni-kl.de

- <sup>1</sup>S. Facsko, T. Dekorsy, C. Koerdt, C. Trappe, H. Kurz, A. Vogt, and H. L. Hartnagel, *Science* **285**, 1551 (1999).
- <sup>2</sup>B. Ziberi, M. Cornejo, F. Frost, and B. Rauschenbach, *J. Phys.: Condens. Matter* **21**, 224003 (2009).
- <sup>3</sup>S. A. Norris, J. Samela, L. Bukonte, M. Backman, F. Djurabekova, K. Nordlund, C. S. Madi, M. P. Brenner, and M. J. Aziz, *Nat. Commun.* **2**, 276 (2011).
- <sup>4</sup>M. Z. Hossain, K. Das, J. B. Freund, and H. T. Johnson, *Appl. Phys. Lett.* **99**, 151913 (2011).
- <sup>5</sup>M. Z. Hossain, J. B. Freund, and H. T. Johnson, *J. Appl. Phys.* **111**, 103513 (2012).
- <sup>6</sup>L. Bischoff, W. Pilz, P. Mazarov, and A. D. Wieck, *Appl. Phys. A* **99**, 145 (2010).
- <sup>7</sup>F. Kollmer, *Appl. Surf. Sci.* **231-232**, 153 (2004).
- <sup>8</sup>D. Debois, A. Brunelle, and O. Lapr evote, *Int. J. Mass Spectrom.* **260**, 115 (2007).
- <sup>9</sup>L. Bischoff, K.-H. Heinig, B. Schmidt, S. Facsko, and W. Pilz, *Nucl. Instrum. Methods Phys. Res., Sect. B* **272**, 198 (2012).
- <sup>10</sup>R. B ottger, L. Bischoff, S. Facsko, and B. Schmidt, *Europhys. Lett.* **98**, 16009 (2012).
- <sup>11</sup>R. B ottger, L. Bischoff, K.-H. Heinig, W. Pilz, and B. Schmidt, *J. Vac. Sci. Technol. B* **30**, 06FF12 (2012).
- <sup>12</sup>R. B ottger, K.-H. Heinig, L. Bischoff, B. Liedke, R. H ubner, and W. Pilz, *Phys. Status Solidi RRL* (2013), doi:10.1002/pssr.201307127.
- <sup>13</sup><http://lammmps.sandia.gov>
- <sup>14</sup>R. W. Olesinski and G. J. Abbaschian, *Bull. Alloy Phase Diagrams* **7**, 535 (1986).
- <sup>15</sup>M. Posselt and A. Gabriel, *Phys. Rev. B* **80**, 045202 (2009).
- <sup>16</sup>M. Yan, M. Sob, D. E. Luzzi, V. Vitek, G. J. Ackland, M. Methfessel, and C. O. Rodriguez, *Phys. Rev. B* **47**, 5571 (1993).
- <sup>17</sup>M. W. Finnis and J. E. Sinclair, *Philos. Mag. A* **50**, 45 (1984); **53**, 161(E) (1986).
- <sup>18</sup>H. Gades and H. M. Urbassek, *Phys. Rev. B* **51**, 14559 (1995).
- <sup>19</sup>J. F. Ziegler, J. P. Biersack, and U. Littmark, *The Stopping and Range of Ions in Solids* (Pergamon, New York, 1985).
- <sup>20</sup>H. J. C. Berendsen, J. P. M. Postma, W. F. van Gunsteren, A. DiNola, and J. R. Haak, *J. Chem. Phys.* **81**, 3684 (1984).
- <sup>21</sup>Y. Wu and R. J. Friauf, *J. Appl. Phys.* **65**, 4714 (1989).
- <sup>22</sup>C. J. Glassbrenner and G. A. Slack, *Phys. Rev.* **134**, A1058 (1964).
- <sup>23</sup>P. H. Keck and W. Van Horn, *Phys. Rev.* **91**, 512 (1953).
- <sup>24</sup>F. Agra and A. Ayyad, *Mater. Lett.* **65**, 760 (2011).
- <sup>25</sup>A. M. Brown and M. F. Ashby, *Acta Metall.* **28**, 1085 (1980).
- <sup>26</sup>A. Miotello and L. F. Don  dalle Rose, *Phys. Lett. A* **87**, 317 (1982).
- <sup>27</sup>R. Vogelsang and C. Hoheisel, *Phys. Rev. A* **38**, 6296 (1988).
- <sup>28</sup>A. Miotello, *J. Phys.: Condens. Matter* **1**, 3363 (1989).
- <sup>29</sup>A. Perronace, G. Ciccotti, F. Leroy, A. H. Fuchs, and B. Rousseau, *Phys. Rev. E* **66**, 031201 (2002).
- <sup>30</sup>S. Duhr and D. Braun, *Proc. Natl. Acad. Sci. USA* **103**, 19678 (2006).
- <sup>31</sup>G. Dominguez, G. Wilkins, and M. H. Thiemens, *Nature (London)* **473**, 70 (2011).
- <sup>32</sup>S. D. Stoddard, *J. Comput. Phys.* **27**, 291 (1978).
- <sup>33</sup>W. Eckstein, *Nucl. Instrum. Methods Phys. Res., Sect. B* **33**, 489 (1988).
- <sup>34</sup>U. Conrad and H. M. Urbassek, *Nucl. Instrum. Methods Phys. Res., Sect. B* **48**, 399 (1990).
- <sup>35</sup>T. J. Colla, R. Aderjan, R. Kissel, and H. M. Urbassek, *Phys. Rev. B* **62**, 8487 (2000).
- <sup>36</sup>K. H. Heinig and L. Bischoff (private communication).
- <sup>37</sup>P. Sigmund, in *Sputtering by Particle Bombardment I*, edited by R. Behrisch (Springer, Berlin, 1981), p. 9.
- <sup>38</sup>U. Conrad and H. M. Urbassek, *Nucl. Instrum. Methods Phys. Res., Sect. B* **61**, 295 (1991).
- <sup>39</sup>H. M. Urbassek, in *Sputtering by Particle Bombardment*, edited by R. Behrisch and W. Eckstein, Vol. 110 of *Topics in Applied Physics* (Springer, Berlin, 2007), p. 189.